# Quadrupole deformation of $^{130}$Xe measured in a Coulomb-excitation experiment

L. Morrison,[1] K. Hadyńska-Klęk,[2,1] Zs. Podolyák,[1] D.T. Doherty,[1] L.P. Gaffney,[3,4] L. Kaya,[5] L. Próchniak,[2] J. Samorajczyk-Pyśk,[2] J. Srebrny,[2] T. Berry,[1] A. Boukhari,[6] M. Brunet,[1] R. Canavan,[1,7] R. Catherall,[4] S.J. Colosimo,[3] J.G. Cubiss,[8] H. De Witte,[9] Ch. Fransen,[5] E. Giannopoulos,[10,4] H. Hess,[5] T. Kröll,[11] N. Lalović,[12] B. Marsh,[4] Y. Martinez Palenzuela,[4,9] P.J. Napiorkowski,[2] G. O'Neill,[13,14] J. Pakarinen,[10] J.P. Ramos,[15,4] P. Reiter,[5] J.A. Rodriguez,[4] D. Rosiak,[5] S. Rothe,[4] M. Rudigier,[1] M. Siciliano,[16,17] J. Snäll,[12] P. Spagnoletti,[18] S. Thiel,[5] N. Warr,[5] F. Wenander,[4] R. Zidarova,[19] and M. Zielińska[16]

[1]*Department of Physics, University of Surrey, Guildford, GU2 7XH, United Kingdom*
[2]*Heavy Ion Laboratory, University of Warsaw, Pasteura 5A, 02-093 Warszawa, Poland*
[3]*Oliver Lodge Laboratory, University of Liverpool, Liverpool, L69 7ZE, United Kingdom*
[4]*CERN, Physics Department, 1211 Geneva 23, Switzerland*
[5]*IKP Köln, Zülpicher Str. 77, 50937 Köln, Germany*
[6]*Université de Paris-Sud 11, 15 Rue Georges Clemenceau, 91400 Orsay, France*
[7]*National Physical Laboratory, Hampton Rd, Teddington, TW11 0LW, United Kingdom*
[8]*Department of Physics, University of York, York ,YO10 5DD, United Kingdom*
[9]*KU Leuven, Instituut voor Kern-en Stralingsfysica, B-3001 Leuven, Belgium*
[10]*Department of Physics, University of Jyväskylä, P.O. Box 35 (YFL), Jyväskylä, FI-40014, Finland*
[11]*GSI Helmholtzzentrum für Schwerionenforschung, Planckstrasse 1, 64291 Darmstadt, Germany*
[12]*Physics Department, Lund University, Box 118, Lund SE-221 00, Sweden*
[13]*Department of Physics and Astronomy, University of the Western Cape, P/B X17, Bellville,ZA-7535, South Africa*
[14]*iThemba LABS, Old Faure Road, Faure, Cape Town, 7131, South Africa*
[15]*SCK CEN, Boeretang 200, 2400 Mol, Belgium*
[16]*IRFU, CEA, Université Paris-Saclay, F-91191 Gif-sur-Yvette, France*
[17]*INFN Laboratori Nazionali di Legnaro, 35020 Legnaro (Pd), Italy*
[18]*School of Computing, Engineering and Physical Sciences, University of the West of Scotland, Paisley PA1 2BE, UK*
[19]*Institut für Kernphysik, Technische Universität Darmstadt, 64289 Darmstadt, Germany*

(Dated: September 29, 2020)

Low-lying states in the isotope $^{130}$Xe were populated in a Coulomb-excitation experiment performed at CERN's HIE-ISOLDE facility. The magnitudes and relative signs of 7 $E2$ matrix elements and 1 $M1$ matrix element coupling 5 low-lying states in $^{130}$Xe were determined using the semiclassical coupled-channel Coulomb-excitation least-squares search code `GOSIA`. The diagonal $E2$ matrix elements of both the $2_1^+$ and $4_1^+$ states were extracted for the first time. The reduced transition strengths are in line with those obtained from previous measurements. Experimental results were compared with the General Bohr Hamiltonian with the microscopic input from mean-field theory utilizing Universal Nuclear Energy Density Functional (UNEDF0), shell-model calculations using the GCN50:82 and SN100PN interactions, and with simple phenomenological models (Davydov-Filippov and $\gamma$-soft). The extracted shape parameters indicate triaxial-prolate deformation in the ground state band. In general, good agreement between theoretical predictions and experimental values was found, while neither phenomenological model was found to provide an adequate description of $^{130}$Xe.

## I. INTRODUCTION

Atomic nuclei often exhibit collective properties, which indicate that when a large number of nucleons are brought together, they are able to form systems acting more like macroscopic objects than ones composed of individual particles. This naturally leads to the idea of a nuclear shape, the determination of which is a key area of nuclear structure research. While nuclei close to magic numbers are known to be spherical, quadrupole-deformed shapes generally prevail throughout the nuclear chart. In particular, studies of how both axially symmetric and axially asymmetric quadrupole shapes evolve across isotopic chains provide key tests of nuclear structure models.

After tin, the xenon isotopic chain, with neutron numbers from $N = 70$ through to $N = 82$ ($^{124-136}$Xe), represents the longest chain of stable isotopes within the nuclear landscape. As such, it is an excellent testing ground for detailed studies of the evolution of nuclear collectivity (and hence deformation) as a function of neutron number. Indeed, the properties of the stable Xe isotopes have been the subject of a number of both experimental and theoretical studies over recent decades. Such studies indicate that while $^{136}$Xe ($N = 82$) appears to be spherical in nature, the structure of the lighter stable Xe isotopes may be strongly influenced by the triaxial (or $\gamma$) degree of freedom [1, 2]. Firm conclusions are, however, significantly hindered by the lack of detailed knowledge on

both spectroscopic quadrupole moments, and on the relative signs of electromagnetic matrix elements, which are critical for evaluating, in a model-independent way, the role of the triaxial degree of freedom in the Xe isotopes. Notably, spectroscopic quadrupole moments have been measured only for the ground states of even-odd $I \neq \frac{1}{2}$ Xe isotopes, as well as for some isomeric states in both odd and even-mass Xe nuclei, however none have previously been reported for short-lived excited states in the Xe isotopes. Thus, the even-even Xe nuclei are the only stable A $\sim$ 130 isotopes where experimental spectroscopic quadrupole moments and the relative signs of electromagnetic matrix elements between low-lying states are unknown [3].

Understanding the evolution of collectivity along an isotopic chain and, in particular, describing the structure of transitional nuclei, has long proved to be a challenge for nuclear theory and nuclear structure models. For the even-even Xe isotopes, past work has focused on calculations employing the General Bohr Hamiltonian [1, 4–6], the nuclear shell model [7], and the interacting boson model (IBM) [8, 9], where the light Xe isotopes have been suggested to represent a transition point between spherical vibrators and $\gamma$-soft rotors, e.g. [10, 11]. In addition, odd-mass nuclei in this region were explored in detail in recent mapped-IBM calculations [8, 9].

Knowledge of this low-lying, low-spin structure may also have important consequences beyond the regime of traditional low-energy nuclear physics. The nucleus $^{130}$Xe is the daughter of a key neutrinoless double beta ($0\nu\beta\beta$) candidate $^{130}$Te, with searches for this decay taking place in experiments around the world, e.g. [12]. As discussed in [13], $0\nu\beta\beta$ decay is expected to take place between initial and final states of similar structure and shape and, consequently, knowledge of low-lying $0^+$ states in $^{130}$Xe is crucial for informing this work.

Safe-energy Coulomb excitation is an experimental method which is able to provide information on the electromagnetic structure of the investigated nucleus by extracting both transitional and diagonal matrix elements, together with their relative signs. Those can be used to determine the shape of individual states using the quadrupole sum rules method, and give unique insight into the properties of a given nucleus. Furthermore, the extracted transition probabilities B($^{E}_{M}\lambda$) provide direct information on the collectivity of the transitions in the investigated nucleus. In this paper, the results of a recent Coulomb-excitation experiment populating states in $^{130}$Xe are presented. The collected data allow for the first examination of the deformation of the $0^+$ ground state and the first excited $2^+$ state in $^{130}$Xe. Furthermore, the extracted set of matrix elements together with their relative signs provides, for the first time, a solid base for an in-depth understanding of the structure of $^{130}$Xe at low excitation energy.

This paper is organized as follows: the experimental details are presented in Sec. II, and the Coulomb-excitation data analysis and experimental results are described in Sec. III. In Sec. IV the theoretical approaches and interpretation are presented together with the quadrupole sum rules analysis.

## II. EXPERIMENTAL DETAILS

A Coulomb-excitation experiment, primarily designed to investigate the singly-magic, two proton-hole nucleus $^{206}$Hg, was performed using the MINIBALL setup at the HIE-ISOLDE facility, CERN. The radioactive $^{206}$Hg beam was found to be contaminated with the isotope of $^{130}$Xe, the origin of which can be attributed to the presence of atomic xenon leaking in from REXTRAP, the xenon having been ionised by charge transfer from the incoming radioactive beam [14]. Therefore, it is not related to the combination of beam and target used in the primary experiment. In order to study the effect of this contaminant, several experimental runs were taken with the lasers responsible for ionizing $^{206}$Hg in the ion source 'turned off', as well as the lasers used within the RILIS, and as such the analysis presented here is solely focused on $^{130}$Xe. The beam composition was checked with an ionisation chamber, confirming no contaminants were present. For more details see Ref [15].

The $^{130}$Xe beam (Q = $29^+$, intensity $\sim$ $3 \times 10^5$ pps), was accelerated using the newly-commissioned HIE-ISOLDE linear accelerator [16, 17], to an energy of 4.195 MeV/u. Post acceleration, it impinged on a 2 mg/cm$^2$ thick $^{94}$Mo target for a total of approximately 7.4 hours. The beam energy fulfilled Cline's safe distance criterion [18], ensuring a purely electromagnetic interaction between the collision partners took place.

Following Coulomb excitation, both the projectile and recoiling target-like particles were detected using an annular Double-Sided Silicon Strip Detector (DSSSD), divided into 16 annular strips on the front side, and a further 24 sectors per individual quadrant, which are coupled into 12 pairs when read out [19, 20]. This high degree of segmentation allowed accurate and precise position identification of the scattered particles.

The energy calibration of the DSSSD detector was carried out for each silicon strip using accelerated stable beams of $^{12}$C, $^{16}$O, $^{20}$Ne and $^{40}$Ar. Additionally, the detector distance from the target, 24.6 mm, was established from the count-rate distribution in a given strip coming from the measured $\alpha$ decay of a $^{226}$Ra source.

The reaction kinematics plot obtained using the DSSSD particle detector is presented in Figure 1. The beam and target recoils are clearly separated for most of the angular range covered by the detector, and were identified by comparing them with simulations performed using the `KINSIM` code [21]. The target particle-like events covered an angular range from 24 to 59° in the labora-

tory frame (LAB), equivalent to 62 to 131° in the center-of-mass system (COM). As presented in Figure 1, the innermost strip of the DSSSD detector is excluded from the analysis because it was not possible to separate the projectile and target-like events in this range. As the experiment was performed in inverse kinematics, the projectile kinematic plot has two solutions corresponding to two different ranges of the center-of-mass frame. However, the full range of projectile-like events is also covered in the target-like events gate, and as such the selection of the $^{94}$Mo and $^{130}$Xe kinematic solutions could be done in an unambiguous way.

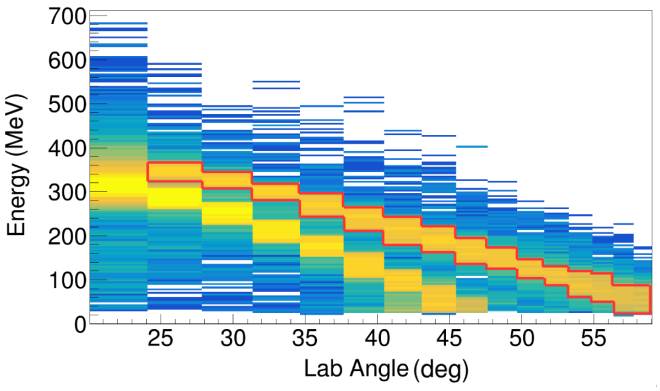


FIG. 1: (Color online) The particle spectrum collected in the DSSSD detector, displaying the projectile and target kinematics for the Coulomb excitation of $^{130}$Xe on a $^{94}$Mo target. The red outline indicates the region gated on for target-like events.

De-excitation $\gamma$ rays were detected by 23 of the total 24 HPGe detectors comprising the MINIBALL array [19]. Energy and efficiency calibrations for the HPGe detectors were undertaken using standard radioactive $^{152}$Eu and $^{133}$Ba sources. The $\gamma$-ray efficiencies were determined using the $\gamma$-ray efficiency code `GREMLIN` [22]. In order to apply the appropriate Doppler-correction, each crystal's precise alignment and positioning was determined from Doppler-shifted $\gamma$ rays following the $(d,p)$ and $(d,n)$ reactions of a stable $^{22}$Ne beam. For more details on the experimental setup and analysis, see Ref. [23].

Both one and two-particle events were included during the data sort given the kinematics of the reaction, allowing for both the target recoil and scattered beam particles to be detected in the angular range covered by the downstream DSSSD detector. In order to select $\gamma$ rays originating from the excitation of either $^{130}$Xe or $^{94}$Mo, only $\gamma$-ray events coincident with a particle were registered, and this particle-$\gamma$ coincidence was subject to time-gating conditions, based on prompt and random events. As seen in Figure 2, the prompt window was set from -300 to 150 ns, and the random window from 250 to 850 ns. These conditions suppress $\gamma$-ray background events associated with activity in the chamber, and allow for a subtraction of random coincidences.

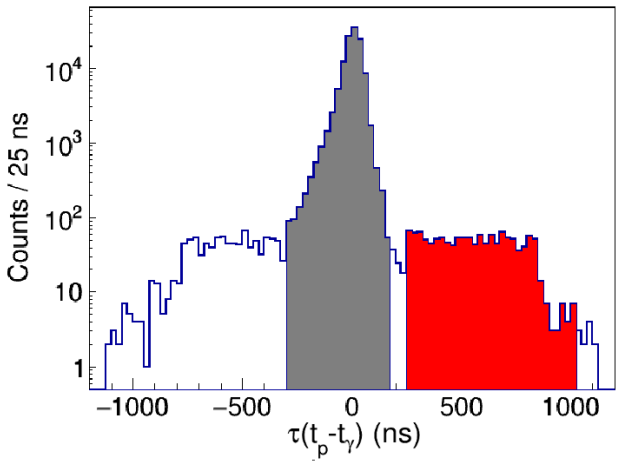


FIG. 2: (Color online) A particle-$\gamma$ coincidence plot showing the time-gating conditions used in the experiment. The peak displays events fulfilling the particle-$\gamma$ coincidence condition. The selected prompt window was 450 ns wide (shown in grey), and the random window was set to 600 ns (shown in red).

By performing the appropriate Doppler-correction for projectile velocity, $\gamma$-ray spectra (recoil-gated Doppler-corrected for projectile-like particles) were produced, as shown in Figure 3. A number of $\gamma$-ray peaks associated with the excitation of $^{130}$Xe [24] are visible in the spectrum. Figure 4 displays a partial level scheme for $^{130}$Xe with transitions relevant to the present study included. The $\gamma$-ray transitions observed in the present experiment are marked in red.

## III. COULOMB-EXCITATION DATA ANALYSIS

The Coulomb-excitation data were analyzed with the semiclassical coupled-channel Coulomb-excitation least-squares search code `GOSIA` [18, 25], in order to extract matrix elements for the observed transitions together with their relative signs and associated uncertainties.

Two normalization methods were used in the Coulomb-excitation analysis. In the first, normalization to the known target properties was performed, as discussed in detail in, e.g., Ref. [26]. Here, this analysis was used only for the first $2_1^+$ state in order to extract the $B(E2; 2_1^+ \rightarrow 0_1^+)$ value in an independent way. The collected data were subdivided into a total of six angular ranges (see Table I): five distinct ones spanning the entire range of angles upon summation, and one total range covering the entire selection of angles at once. The number of subdivisions was limited in order to ensure sufficient statistics in the $2_1^+ \rightarrow 0_1^+$ transitions in both $^{130}$Xe and $^{94}$Mo, and each range was taken with weight 0.5, ensuring every event was only counted once. In $^{94}$Mo, both the

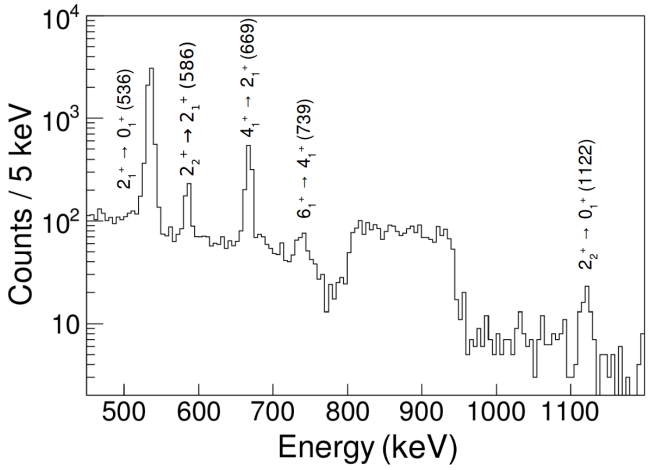


FIG. 3: (Color online) The particle-particle-$\gamma$ coincidence spectrum collected in the Coulomb excitation of a $^{130}$Xe beam on a $^{94}$Mo target experiment, gated on the recoil-like particles, Doppler-corrected for the $^{130}$Xe projectile velocity. All observed transitions in the Coulomb-excited $^{130}$Xe are labeled. The energy region in the spectrum between 800 and 950 keV corresponds to the Doppler-broadened $2^+_1 \rightarrow 0^+_1$ transition at 871 keV in the $^{94}$Mo target.

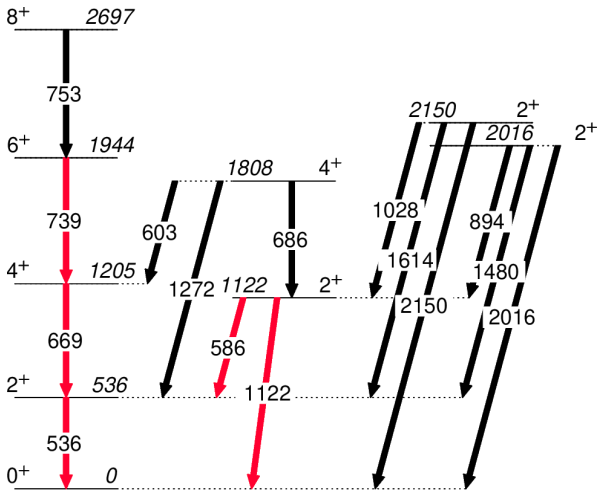


FIG. 4: (Color online) Low-lying excited states in $^{130}$Xe, considered in the present analysis. Transitions observed in the current experiment with a $^{94}$Mo target are marked in red. Level and transition energies are given in keV.

reduced transition strength (B($E2$; $2^+_1 \rightarrow 0^+_1$) = 16.0(4) W.u.), and the spectroscopic quadrupole moment of the $2^+_1$ state ($Q_s(2^+_1)$ = -0.13(8) eb), are known to good precision [27], and consequently, this information could be used to normalize data from the different angular ranges. The B($E2$; $2^+_1 \rightarrow 0^+_1$) value for the $^{130}$Xe beam could then be extracted from the two-dimensional $\chi^2$ surface map, calculated using the GOSIA2 program together with a specially-developed $\chi^2$ surface code [28], by performing a minimization with respect to the $|\langle 2^+_1 \| E2 \| 0^+_1 \rangle|$ and $|\langle 2^+_1 \| E2 \| 2^+_1 \rangle|$ matrix elements. This analysis yielded a $B(E2; 2^+_1 \rightarrow 0^+_1) = 30(+2,-7)$ W.u., in good agreement with previous work [3, 11, 29–31, 33], but with a significant uncertainty on the extracted quadrupole moment.

In addition to the analysis performed on the beam particles, an additional analysis was carried out for the target peaks, by Doppler-correcting for $^{94}$Mo. A significant amount of $^{95}$Mo was discovered to be present in the target, accounting for 5(1)% of the total statistics. Additional excitation due to this target contamination was accounted for by increasing the uncertainty values for all $\gamma$-ray yields by 5%, when input into GOSIA.

The analysis described above gives confidence in the reported literature values for the $2^+_1 \rightarrow 0^+_1$ transition probability. Consequently, here, in order to extract a full set of matrix elements from the experimental data using the standard GOSIA code, the normalization of the data was performed with the lifetime of the $2^+_1$ state. The most recent and precise lifetime value of $\tau = 14.7(3)$ ps [29, 30] was chosen, which corresponds to a B($E2$) of 32(1) W.u. The additional precision of this value, compared to the one obtained in the GOSIA2 analysis, increases the sensitivity to second-order effects and, as a result, improves the precision of the extracted matrix elements. The GOSIA analysis also incorporates other spectroscopic information such as $\gamma$-ray branching and $E2/M1$ mixing ratios, and the lifetimes of low-lying states (see Table II). This information serves to constrain the final GOSIA analysis and enters the multidimensional $\chi^2$ function fit in the same way as the measured $\gamma$-ray intensities. Two further, unobserved, $2^+$ states, at excitation energies of 2016 and 2150 keV, were also included in the GOSIA analysis. This was in order to account for the possible excitation of these unobserved levels in the measured $\gamma$-ray yields. The known spectroscopic data for these states were included (see Table II), as well as the known matrix elements, from Ref. [11], to serve as additional constraints. However, in the analysis, the unknown $Q_s$ of these two states were set to 0.

The data were again subdivided into 6 angular ranges (as presented in Table I), in order to exploit the scattering angle dependence of the Coulomb-excitation cross section and enable spectroscopic quadrupole moments to be extracted. A $\chi^2$ fit of the observed $\gamma$-ray yields (Table I) and other spectroscopic data (Table II) was performed with 15 $E2$ and 2 $M1$ matrix elements. A sign convention was adopted where the signs of all in-band transitional $E2$ matrix elements were assumed to be positive, as well as that of the $\langle 0^+_1 \| E2 \| 2^+_2 \rangle$ transition; the signs of all other $E2$ matrix elements were then determined relative to those.

The statistical errors of the matrix elements were determined when convergence of the $\chi^2$ minimization was achieved. This was performed in two steps. Firstly, in order to find the 'diagonal' uncertainty, the $\chi^2$ surface is sampled in the vicinity of the minimum, using different

TABLE I: Numbers of counts in the observed $\gamma$-ray transitions in $^{130}$Xe used in the presented data analysis. In addition, the number of counts in the observed $2_1^+ \rightarrow 0_1^+$ $\gamma$-ray transition in $^{94}$Mo (871 keV), for different angular ranges used in the target normalization approach analysis described in the text, is included.

| | | $^{130}$Xe | | $^{94}$Mo | |
|---|---|---|---|---|---|
| $I_i^\pi$ | $I_f^\pi$ | $E_\gamma$ (keV) | Counts | $E_\gamma$ (keV) | Counts |
| Total spectrum ($\theta_{CM} = 62 - 131°$) | | | | | |
| $2_1^+$ | $0_1^+$ | 536 | 5710(286) | 871 | 1720(43) |
| $4_1^+$ | $2_1^+$ | 669 | 900(45) | | |
| $6_1^+$ | $4_1^+$ | 739 | 151(22) | | |
| $2_2^+$ | $2_1^+$ | 586 | 298(24) | | |
| $2_2^+$ | $0_1^+$ | 1122 | 51(9) | | |
| $\theta_{CM} = 111 - 131°$ | | | | | |
| $2_1^+$ | $0_1^+$ | 536 | 754(29) | 871 | 243(17) |
| $4_1^+$ | $2_1^+$ | 669 | 195(15) | | |
| $6_1^+$ | $4_1^+$ | 739 | 39(9) | | |
| $2_2^+$ | $2_1^+$ | 586 | 81(11) | | |
| $\theta_{CM} = 94 - 110°$ | | | | | |
| $2_1^+$ | $0_1^+$ | 536 | 1294(65) | 871 | 375(21) |
| $4_1^+$ | $2_1^+$ | 669 | 260(18) | | |
| $2_2^+$ | $2_1^+$ | 586 | 81(12) | | |
| $\theta_{CM} = 85 - 93°$ | | | | | |
| $2_1^+$ | $0_1^+$ | 536 | 1018(51) | 871 | 224(16) |
| $4_1^+$ | $2_1^+$ | 669 | 198(16) | | |
| $2_2^+$ | $2_1^+$ | 586 | 63(10) | | |
| $\theta_{CM} = 74 - 84°$ | | | | | |
| $2_1^+$ | $0_1^+$ | 536 | 1039(52) | 871 | 277(18) |
| $4_1^+$ | $2_1^+$ | 669 | 121(13) | | |
| $2_2^+$ | $2_1^+$ | 586 | 44(10) | | |
| $\theta_{CM} = 62 - 73°$ | | | | | |
| $2_1^+$ | $0_1^+$ | 536 | 1540(77) | 871 | 420(21) |
| $4_1^+$ | $2_1^+$ | 669 | 111(13) | | |
| $2_2^+$ | $2_1^+$ | 586 | 45(11) | | |

values of the matrix element in question, with all other matrix elements remaining fixed. Secondly, in order to obtain the total statistical uncertainty, all of the possible correlations between matrix elements are accounted for. As a result, a set of five $E2$ and one $M1$ transitional matrix elements was extracted, connecting five low-lying states in $^{130}$Xe. Similarly, two spectroscopic quadrupole moments were determined, for the first time, from the extracted diagonal matrix elements. The experimental results are presented in Tables III and IV, where they are compared with both literature values and the results of theoretical calculations.

The set of reduced matrix elements obtained reproduces all of the lifetimes, branching, and mixing ratios

TABLE II: The $\gamma$-ray branching ratios, mixing ratios, $\delta$, for mixed $E2/M1$ transitions, and the lifetimes of the excited states in $^{130}$Xe used as additional data points in the Coulomb-excitation data analysis. The $2_2^+ \rightarrow 2_1^+$ and $4_2^+ \rightarrow 4_1^+$ mixing ratio values are from Refs. [34, 35], and the $\gamma$-ray branching ratios were calculated using data from Ref. [3]. The lifetimes are from Refs. [29, 30].

| $I_i^\pi$ | $I_j^\pi$ | $E_\gamma$ (keV) | Branching ratio |
|---|---|---|---|
| $2_2^+$ | $2_1^+$ | 586 | 1 |
| $2_2^+$ | $0_1^+$ | 1122 | 0.15(1) |
| $4_2^+$ | $2_2^+$ | 686 | 1 |
| $4_2^+$ | $4_1^+$ | 603 | 0.58(5) |
| $4_2^+$ | $2_1^+$ | 1272 | 0.70(6) |
| $2_4^+$ | $0_1^+$ | 2150 | 0.047(2) |
| $2_4^+$ | $2_2^+$ | 1028 | 0.087(4) |
| $2_4^+$ | $2_1^+$ | 1614 | 1 |
| $I_i^\pi$ | $I_j^\pi$ | $E_\gamma$ (keV) | $\delta(E2/M1)$ |
| $2_2^+$ | $2_1^+$ | 586 | 3.75(12) |
| $4_2^+$ | $4_1^+$ | 603 | 2.4(+13,-7) |
| State | | Energy (keV) | $\tau$(ps) |
| $2_1^+$ | | 536 | 14.7(3) |
| $4_1^+$ | | 1205 | 3.3(2) |
| $6_1^+$ | | 1944 | 1.9(7) |
| $2_2^+$ | | 1122 | 6.5(6) |

presented in Table II within a $1\sigma$ uncertainty. Furthermore, good agreement is found between the reduced transition strength results obtained here and previously published results (Table III). We note that in addition to the $B(E2)$ transition strengths, the $B(M1; 2_2^+ \rightarrow 2_1^+)$ value could also be extracted owing to the experimentally determined $\delta$(E2/M1) mixing ratio [31] for this $\gamma$ ray.

The spectroscopic quadrupole moments for the $2_1^+$ and $4_1^+$ states in $^{130}$Xe were determined for the first time (Table IV). Both the $2_1^+$ and $4_1^+$ signs and values ($Q_s(2_1^+) = -0.38(+17, -14)$ e.b. and $Q_s(4_1^+) = -0.41(12)$ e.b.), indicate stable prolate deformation within the yrast band. Furthermore, these moments are reduced with respect to those calculated with a simple rotor model, fit to the experimental $B(E2; 2_1^+ \rightarrow 0_1^+)$ value, ($Q_s(2_1^+) = -0.7$ e.b., $Q_s(4_1^+) = -0.9$ e.b.), suggesting an influence from the $\gamma$ degree of freedom. However, these moments, as well as the reduced transition probabilities in the ground-state band, are only weakly affected by $\gamma$ deformation so, in order to draw more definitive conclusions, a detailed theoretical analysis was undertaken.

## IV. DISCUSSION

Attempts to describe the structure of the mass A$\sim$130 nuclei theoretically invoke both single-particle shell-

TABLE III: Reduced transition strengths, B($E2; I_i^+ \to I_f^+$) and B($M1; I_i^+ \to I_f^+$) in $^{130}$Xe extracted from the present experiment. Previous experimental values are also given; these are based on lifetime measurements [3, 29–31] and Coulomb-excitation experiments [11, 33]. Theoretical values obtained with the collective GBH-UNEDF0 model, as well as the GCN50:82 and SN100PN shell-model interactions are shown. For the shell model theoretical calculations, different sets of effective charges were used, as indicated. For the $2_2^+ \to 2_1^+$ transition, the theoretical $B(M1)$ values were obtained using effective $g$ factor values of: $g_{l,p} = 1$, $g_{l,n} = 0$, $g_{s,p} = 3.91$, $g_{s,n} = -2.68$. The last two columns contain the values from the Davydov-Filipov model (D-F), and $\gamma$-soft model.

| | | | B($E2; I_i^+ \to I_f^+$) (W.u.)[a] | | | | | | | | | |
|---|---|---|---|---|---|---|---|---|---|---|---|---|
| | | | | | | GCN50:82 | | SN100PN | | | |
| $I_i^+ \to I_f^+$ | $E_\gamma$ (keV) | $\langle I_i \| E2 \| I_f \rangle$ (eb) | Present | Previous | GBH-UNEDF0 | $e_\pi = 1.5e$ $e_\nu = 0.5e$ | $e_\pi = 1.53e$ $e_\nu = 0.945e$ | $e_\pi = 1.5e$ $e_\nu = 0.5e$ | $e_\pi = 1.68e$ $e_\nu = 0.84e$ | D-F | $\gamma$-soft |
| $2_1^+ \to 0_1^+$ | 536 | 0.79(4) | 32(3) | 37.1(17) [31]<br>38(5) [3]<br>30.0(+44, −28) [33]<br>33.2(26) [32]<br>32(1) [29, 30] | 24 | 21 | 35 | 20 | 35 | 32 | 36 |
| $4_1^+ \to 2_1^+$ | 669 | 1.29(6) | 47(4) | 44.5(20) [31]<br>46.4(46) [11]<br>47(6) [29, 30] | 46 | 32 | 51 | 31 | 52 | 46 | 61 |
| $6_1^+ \to 4_1^+$ | 739 | 1.74(+21, −18) | 60(−12, +14) | 69(9) [11]<br>51(40) [30] | 64 | 31 | 48 | 18 | 29 | 56 | 84 |
| $2_2^+ \to 0_1^+$ | 1122 | 0.067(3) | 0.23(2) | 0.24(2) [31]<br>0.28(5) [11]<br>0.25(5) [30] | 0.30 | 0.10 | 0.40 | 0.10 | 0.20 | 2.00 | 0.02 |
| $2_2^+ \to 2_1^+$ | 586 | 0.85(4) | 37(3) | 37.1(28) [31]<br>44.3(81) [11]<br>38(7) [30] | 35 | 22 | 38 | 26 | 46 | 21 | 61 |

| | | | B($M1; I_i^+ \to I_f^+$) (W.u.)[b] | | | | | | |
|---|---|---|---|---|---|---|---|---|---|
| | | | | | | GCN50:82 | SN100PN | | |
| $I_i^+ \to I_f^+$ | $E_\gamma$ (keV) | $\langle I_i \| M1 \| I_f \rangle (\mu)$. | Present | Previous | GBH-UNEDF0 | $g_{l(p,n)} = 1, 0$ ; $g_{s(p,n)} = 3.91, -2.68$ | | D-F | $\gamma$-soft |
| $2_2^+ \to 2_1^+$ | 586 | 0.11(1) | 0.0014(2) | 0.0014(2) [31] | – | 0.0004 | 0.0020 | – | – |

[a]For an $E2$ transition in $^{130}$Xe, 1 Wu = $3.912 \times 10^{-3}$ $e^2$b$^2$
[b]For an $M1$ transition in $^{130}$Xe, 1 Wu = 1.79 $\mu^2$

TABLE IV: Spectroscopic quadrupole moments, $Q_s$ extracted for $^{130}$Xe compared with theoretical calculations obtained with the collective GBH-UNEDF0 model, the GCN50:82 and SN100PN shell-model interactions, Davydov-Filipov model (D-F) and the $\gamma$-soft model. The used effective charges are indicated. $Q_s < 0$ indicates prolate deformation and $Q_s > 0$ indicates oblate deformation. The intrinsic quadrupole moments ($Q_0$), calculated from the diagonal matrix elements obtained in the present experiment assuming rigid axially symmetric rotor and K=0, are given in the last column.

| Level | $\langle I\|\|E2\|\|I\rangle$ (eb) | $Q_s$ (eb) | | | | | | | | $Q_0$ (eb) |
|---|---|---|---|---|---|---|---|---|---|---|
| | | | | GCN50:82 | | SN100PN | | D-F | $\gamma$-soft | |
| | | Present | GBH-UNEDF0 | $e_\pi = 1.5e$ $e_\nu = 0.5e$ | $e_\pi = 1.53e$ $e_\nu = 0.945e$ | $e_\pi = 1.5e$ $e_\nu = 0.5e$ | $e_\pi = 1.68e$ $e_\nu = 0.84e$ | | | |
| $2_1^+$ | $-0.50(+22,-18)$ | $-0.38(+17,-14)$ | $-0.35$ | $-0.35$ | $-0.42$ | $-0.20$ | $-0.25$ | -0.55 | -0.04 | $1.33(+60,-49)$ |
| $4_1^+$ | $-0.55(16)$ | $-0.41(12)$ | $-0.47$ | $-0.53$ | $-0.64$ | $-0.53$ | $-0.64$ | -0.42 | -0.07 | 1.13(33) |
| $2_2^+$ | 0.1(1) | 0.1(1) | 0.31 | 0.34 | 0.41 | 0.20 | 0.24 | 0.55 | 0.02 | -0.3(3) |

model calculations and beyond mean field approaches. Of these nuclei, the stable Xe isotopes are amongst the most challenging to describe, owing to the gradual shape transition from $\gamma$-soft structures in the lighter nuclei through to spherical $^{136}$Xe at the $N = 82$ shell closure. For the odd-A isotopes, positive spectroscopic quadrupole moments have been reported for low-lying states in $^{133,135}$Xe, following colinear laser spectroscopy experiments [36], indicating oblate deformation. This is in contrast to the lighter $^{131}$Xe isotope, where modest prolate deformation prevails [36].

Here, in order to aid the interpretation of the experimental results, theoretical calculations were performed with a mean-field formalism, which is well suited to describing nuclear collectivity, a large-scale shell-model approach, with two different interactions, as well as a simple Davydov Filippov (rigid triaxial) model [37], and a $\gamma$-soft model based on a Hamiltonian with $\gamma$-independent potential energy and a constant mass parameter [2, 38]. In addition, the quadrupole sum rules method, which links $E2$ matrix elements to deformation parameters defined in the intrinsic frame of the nucleus, is applied in order to extract shape invariants ($\beta$,$\gamma$), allowing for conclusions on the shapes of low-lying states to be made and an in-depth comparison with theory.

### General Bohr Hamiltonian based on microscopic mean-field theory

The first theoretical approach utilized (considering the effects of low-energy collectivity), can be described as applying the General Bohr Hamiltonian (GBH) with the microscopic input from the mean-field theory utilizing the Universal Nuclear Energy Density Functional (UNEDF0) [39]. The method used to construct the collective Hamiltonian (GBH) is based on the adiabatic time-dependent Hartree-Fock-Bogolyubov (HFB) (ATDHFB) theory. Details of the method can be found in Refs. [1, 40–42]. The GBH-UNEDF0 functional is a Skyrme-type 'standard' functional in the particle-hole channel with the spin-orbit term taken as in the SkI parametrisation [43], while the pairing interaction is a sum of the standard volume and density-dependent surface-peaked $\delta$ interaction. The fitting of proton and neutron pairing strengths is done simultaneously with other functional parameters. All these parameters are fixed for the whole nuclear table. The Lipkin-Nogami (LN) method is applied in order to avoid pairing for magic nuclei and their neighbors 'collapsing'. It should be noted that in the GBH-UNEDF0 approach no fitting of the effective charges is performed.

The GBH-UNEDF0 calculations were performed for the even-even $^{118-144}$Xe isotopes [1]. The low-energy spectra and $B(E2; 4^+ \rightarrow 2^+)$ transition probabilities were found to be in relatively good agreement with available experimental data, with the largest discrepancies around the semi-magic $^{136}$Xe nucleus. One should note that this was achieved after scaling all mass parameters by a factor of 1.3, needed mainly to reproduce the energy spectra (the effect on the transition strengths is much smaller). This is a common procedure; for its origin see [1] and references herein.

The GBH-UNEDF0 energy level scheme is compared with the experimental one in Figure 6. The results of the GBH-UNEDF0 calculations for $^{130}$Xe for transition strengths and quadrupole moments, are compared with experimental values in Tables III and IV, respectively (microscopic calculations for the $M1$ transitions are not yet implemented so no B($M1$) values are determined). Furthermore, it should be pointed out that the agreement with experimental values is very good for the quadrupole moments.

The potential-energy surface map for the $^{130}$Xe ground state is shown in Figure 5, which indicates a pronounced $\gamma$ softness for $\beta$ ranging from 0 up to 0.3 where the potential starts to increase.

The theoretical shape parameters from GBH-UNEDF0

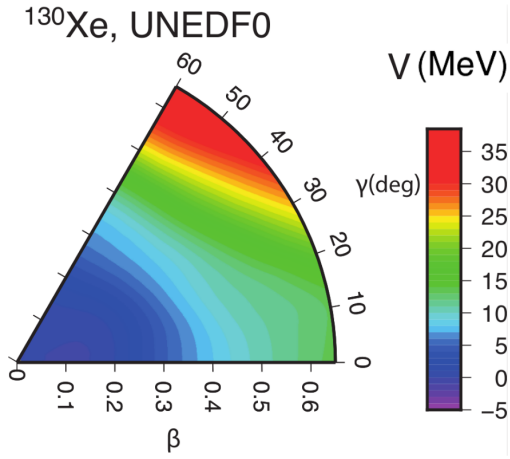


FIG. 5: (Color online) Potential energy surface map (relative to a spherical shape value) for the ground state of $^{130}$Xe, computed using the GBH-UNEDF0 functional. A pronounced $\gamma$-soft shape is visible for $\beta$ ranging from 0 up to 0.3.

calculations are further compared to the experimental ones in Table V.

### Large-scale shell model calculations

Large-scale shell model calculations were performed with two different interactions: GCN50:82 [44] and SN100PN [45]. Both interactions make use of a valence space consisting of all proton and neutron orbitals between the magic shell number closures $N = Z = 50$ and $N = Z = 82$. Therefore, $^{100}$Sn is considered to be an inert core. $^{130}$Xe has a large number of valence particles, with 4 protons and 6 neutron holes relative to the $Z = 50$ and $N = 82$ shell closures.

The SN100PN interaction utilizes the jj55pna Hamiltonian [45] within the `NUSHELLX@MSU` [46] code. The Hamiltonian itself treats four types of interactions separately: neutron-neutron, neutron-proton, proton-proton and Coulomb-proton repulsion. The two-body interaction is based on a renormalized $G$ matrix (itself derived from the CD-Bonn nucleon-nucleon interaction). The single-particle proton and neutron energies are taken from the experimental levels of $^{133}$Sb and $^{131}$Sn.

The GCN50:82 interaction [44] is also based on a realistic $G$ matrix (derived from the CD-Bonn potential). However two-body matrix elements were modified by normalizing to sets of experimental excitation energies in even-even and even-odd semi-magic nuclei, even-odd Sb isotopes and $N = 81$ isotones, and some known odd-odd nuclei around $^{132}$Sn. The calculations were undertaken using the `KSHELL` program [47].

Both shell model approaches have successfully reproduced experimental results for a range of isotopes in this mass region, namely $^{135,136,137}$Ba and $^{131,132,133,135}$Xe [31, 44, 48–51]. In particular, the GCN50:82 interaction shows good agreement for the neighboring Xe isotopes $^{131}$Xe [48], $^{132}$Xe [49] and $^{133}$Xe [50].

The experimental and shell model excited states for $^{130}$Xe are compared in Figure 6. There is a fair agreement, however the experimental energies are typically lower than their theoretical counterparts, for both interactions. The higher theoretical values for the yrast $2^+$ and $4^+$ states probably indicate that in reality the wave functions are more fragmented. The higher experimental $E(4^+)/E(2^+)= 2.25$ ratio, compared to the theoretical ratios 2.12 (GCN50:82) and 2.17 (SN100PN), suggests the same.

The experimental transition strengths and spectroscopic quadrupole moments are compared with those of the shell-model calculations in Tables III and IV. When using the standard effective charges of $e_\nu = 0.5e$ and $e_\pi = 1.5e$, the shell-model reduced transition strengths are too low. For example, the $B(E2; 2_1^+ \rightarrow 0_1^+)$ is 21 and 20 W.u. for the GCN50:82 and the SN100PN interactions, respectively, which are roughly a factor of 1.5 below the experimental value. Previous studies used larger effective charges for nuclei in this region of the nuclear chart. For example, transition strengths from isomeric decays in $^{129}$Sn, $^{131}$Te, $^{133}$Xe, $^{135}$Ba were described using $e_\pi = 1.52e$ and $e_\nu = 0.81e$ in both the GCN50:82 and the SN100PN interactions [50]. The same effective charges were used for $^{133}$Te, $^{135}$Xe and $^{137}$Ba with the SN100PN interaction [52]. Here for the case of $^{130}$Xe, which has a larger number of valence nucleons than any of the aforementioned nuclei, we use slightly higher effective charges: $e_\pi = 1.53$ and $e_\nu = 0.945$ for the GCN50:82 interaction, and $e_\pi = 1.68$ and $e_\nu = 0.84$ for the SN100PN interaction. These neutron charges were chosen to reproduce the $B(E2; 2_1^+ \rightarrow 0_1^+)$ value in $^{126}$Sn [53]. Keeping the neutron charge fixed, the proton charge was modified to reproduce the $B(E2; 2_1^+ \rightarrow 0_1^+)$ value in $^{128}$Te [24].

The known magnetic dipole moments in $^{130}$Xe were also well reproduced by the shell model calculations. This is not surprising, since the SN100PN interaction was originally developed to explore the magnetic moments in Sb and Te isotopes [45]. Using effective $g$ factors $g_{l,p} = 1.0$, $g_{l,n} = 0.0$, $g_{s,p} = 3.91$, and $g_{l,n} = -2.68$ (also used for the $B(M1)$ calculations), the following results were obtained: $\mu(2_1^+) = +0.78$, $\mu(4_1^+) = +1.83$, and $\mu(2_2^+) = +1.83$ for the GCN50:82 interaction, and $\mu(2_1^+) = +0.58$, $\mu(4_1^+) = +1.57$, and $\mu(2_2^+) = +0.59$ for the SN100PN interaction. These compare well with the experimental values of $\mu(2_1^+) = +0.67(2)$, $\mu(4_1^+) = +1.7(2)$, and $\mu(2_2^+) = +0.9(2)$ [54]. All values are given in units of nuclear magnetons.

The theoretical spectroscopic quadrupole moments are also compared with those measured during this study, as shown in Table IV. The signs of the extracted spectroscopic quadrupole moments are theoretically reproduced

for both states.

Both the larger predicted energies, and the need to make use of greater than usual effective charges to reproduce the transition strengths, indicate that the utilized model space is not large enough to reproduce the collective nature of $^{130}$Xe. Cross-shell excitations would need to be considered in order to get a better agreement. Presently, these would be too computationally extensive, and have, therefore, not been performed to date. Nevertheless, the good reproduction of present data using shell model theory for a nucleus with ten valence particles is quite remarkable.

### Quadrupole Sum Rules

In order to extract information on the charge distribution of the nucleus in specific states from the measured $E2$ matrix elements, the quadrupole sum rules method [18, 55–57] can be used. This method is based on the fact that the electric multipole transition operator $E(\lambda{=}2,\ \mu)$ is a spherical tensor and can be represented using two parameters: $Q$, the overall quadrupole deformation parameter equivalent to the elongation parameter $\beta$ in Bohr's model, and $\delta$, which is related to the triaxiality parameter $\gamma$.

The expectation values of the lowest-order quadrupole rotational invariants $\langle Q^2\rangle$ and $\langle Q^3\cos(3\delta)\rangle$ describe the deformation of individual states in both the intrinsic and laboratory frames. While the first of the presented invariants is a measure of overall quadrupole deformation and can be extracted using the absolute values of the $E2$ matrix elements, the higher-order invariant $\langle Q^3\cos(3\delta)\rangle$, that provides information on triaxial asymmetry, strongly depends on the relative signs of the relevant $E2$ matrix elements.

The $E2$ matrix elements extracted in the present analysis were used to determine the deformation parameters of the ground state, $\langle Q^2\rangle$ and $\langle\cos(3\delta)\rangle$. Here, the contribution of the unobserved $2^+$ states was also taken into account by including the matrix elements from Ref. [11], however, the unknown diagonal matrix elements of these two states were set to 0.

For this discussion, it should be noted that the uncertainty on the $\langle 2_2^+||E2||2_2^+\rangle$ diagonal matrix element extracted here was of the order 100% (0.1(1) eb). However, due to the observed sensitivity to the sign of this matrix element in the analysis, it was still possible to evaluate the ($\beta$,$\gamma$) deformation parameters for the ground state with confidence, with the error bar on the final values reflecting this uncertainty.

The results of the experimental sum rule analysis are given, together with theoretical values, in Table V. The shell-model results were obtained by applying the quadrupole sum rules to the theoretical matrix elements, while the GBH-UNEDF0 results are obtained directly from the calculations. Here, however, the contribution of the $E2\times E2$ and $E2\times E2\times E2$ components, calculated from the theoretical matrix elements, is also presented. It should be noted that the shape invariants calculated this way agree well with the ones extracted directly from the wave functions. Moreover, only the first two $2^+$ states are accounted for in the calculations of the shell-model shape invariants, and in the case of the GBH-UNEDF0 ones, the first three $2^+$ states. The missing loops are marked with '–'. Although the present experiment did not yield the $\langle 2_2^+||E2||2_2^+\rangle$ value, the contribution to the deformation of the ground state is negligible. The contribution of the higher lying $2^+$ states is also small as the more significant components in both shape invariants come from the excitation of the $2_1^+$ state. This experimental effect is supported by all the presented theoretical models.

The obtained quadrupole shape invariants were then converted to $\beta$ and $\gamma$ deformation parameters. The experimental deformation parameters for the ground state correspond to values of $\beta = 0.17(2)$ and $\gamma = 23(5)^\circ$, indicating a triaxial-prolate shape for the ground state. Additionally, in the course of the present data analysis, it was possible to extract the quadrupole deformation parameter $\langle Q^2\rangle$=0.66(4) e$^2$b$^2$ of the $2_1^+$ state, which corresponds to $\beta$=0.17(2), as presented in Table V.

### Phenomenological models

#### *Davydov-Filippov model*

The experimental results and those from the shell model and mean field theoretical predictions were further compared to results obtained with the rigid triaxial-rotor model of Davydov and Filippov [37, 58]. This model represents a general phenomenological approach for quadrupole nuclear deformations where the nuclear deformation $\beta$, and asymmetry parameter $\gamma$, are considered to be fixed parameters for a given nucleus with $\gamma \neq 0$; and not as dynamic variables as in the General Bohr Hamiltonian model. Using the experimental energy of the $2_1^+$ state (536 keV) and the measured $\beta$=0.17 and $\gamma$=23° values, a set of matrix elements was calculated using the DF: Davydov-Filippov Code [59]. The resulting transition probabilities and quadrupole moments are compared in Tables III and IV, and the theoretical level scheme is presented in Figure 6. In general, good agreement is observed for in-band matrix elements. However, the large transitional matrix element coupling the $2_2^+$ state to the $2_1^+$ one is not borne out in the calculations, which is probably a consequence of the $\gamma$-rigid nature of the model. Similarly, the $2_2^+ \rightarrow 0_1^+$ transition strength is over predicted.

The evolution of the $\langle 2_1^+||E2||2_1^+\rangle$ to $\langle 2_1^+||E2||0_1^+\rangle$ ratio with $\gamma$ deformation, calculated with the Davydov-Filippov model, is shown in Figure 7. These results are

TABLE V: Experimental and theoretical quadrupole shape invariants: $\langle Q^2 \rangle$ and $\langle \cos(3\delta) \rangle$ for $0_1^+$ states in $^{130}$Xe. The contribution of the individual matrix elements to the final values of $\langle Q^2 \rangle$ is shown. The $\langle Q^2 \rangle$ invariant is formed by summing all the contributions and by multiplying the sum by 1 and by $-0.873$ for $\langle \cos(3\delta) \rangle$ [41, 57]. The loops containing transitional matrix elements are included twice in the contribution to the $\langle \cos(3\delta) \rangle$ invariant as their zero-coupled products can be formed in two possible ways. Experimental results not obtained in the present work are from Ref [11], while the relative signs between matrix elements were adopted from the GBH calculations if they could not be determined in this analysis.

| | | Experiment | GBH-UNDF0 | GCN50:82 $e_\pi = 1.5e$ $e_\nu = 0.5e$ | GCN50:82 $e_\pi = 1.53e$ $e_\nu = 0.945e$ | SN100PN $e_\pi = 1.5e$ $e_\nu = 0.5e$ | SN100PN $e_\pi = 1.68e$ $e_\nu = 0.84e$ | $\gamma$-soft |
|---|---|---|---|---|---|---|---|---|
| State | Component $E2 \times E2$ | | | Contribution to $\langle Q^2 \rangle$ (e$^2$fm$^4$) | | | | |
| $0_1^+$ | $\langle 0_1^+ \|\| E2 \|\| 2_1^+ \rangle \langle 2_1^+ \|\| E2 \|\| 0_1^+ \rangle$ | 6240 | 4750 | 4170 | 6760 | 4000 | 6850 | 6980 |
| | $\langle 0_1^+ \|\| E2 \|\| 2_2^+ \rangle \langle 2_2^+ \|\| E2 \|\| 0_1^+ \rangle$ | 45 | 50 | 20 | 80 | 10 | 30 | 5 |
| | $\langle 0_1^+ \|\| E2 \|\| 2_3^+ \rangle \langle 2_3^+ \|\| E2 \|\| 0_1^+ \rangle$ | 20 | 2 | – | – | – | – | 40 |
| | $\langle 0_1^+ \|\| E2 \|\| 2_4^+ \rangle \langle 2_4^+ \|\| E2 \|\| 0_1^+ \rangle$ | 45 | – | – | – | – | – | 0 |
| | $\langle Q^2 \rangle$ | 6350(400) | 4800 | 4190 | 6840 | 4000 | 6880 | 7030 |
| | $\langle \beta \rangle$ | 0.17(2) | 0.15 | 0.14 | 0.17 | 0.13 | 0.17 | 0.18 |
| $2_1^+$ | $\langle 2_1^+ \|\| E2 \|\| 0_1^+ \rangle \langle 0_1^+ \|\| E2 \|\| 2_1^+ \rangle$ | 1250 | 950 | 830 | 1350 | 800 | 1370 | 1400 |
| | $\langle 2_1^+ \|\| E2 \|\| 2_2^+ \rangle \langle 2_2^+ \|\| E2 \|\| 2_1^+ \rangle$ | 1440 | 1350 | 870 | 1500 | 1030 | 1800 | 2380 |
| | $\langle 2_1^+ \|\| E2 \|\| 2_3^+ \rangle \langle 2_3^+ \|\| E2 \|\| 2_1^+ \rangle$ | 35 | 10 | – | – | – | – | 1 |
| | $\langle 2_1^+ \|\| E2 \|\| 2_4^+ \rangle \langle 2_4^+ \|\| E2 \|\| 2_1^+ \rangle$ | 5 | – | – | – | – | – | 0 |
| | $\langle 2_1^+ \|\| E2 \|\| 4_1^+ \rangle \langle 4_1^+ \|\| E2 \|\| 2_1^+ \rangle$ | 3350 | 3200 | 2270 | 3580 | 2160 | 3630 | 4300 |
| | $\langle 2_1^+ \|\| E2 \|\| 4_2^+ \rangle \langle 4_2^+ \|\| E2 \|\| 2_1^+ \rangle$ | 25 | 0 | 1250 | 25 | 1 | 0 | 2 |
| | $\langle 2_1^+ \|\| E2 \|\| 4_3^+ \rangle \langle 4_3^+ \|\| E2 \|\| 2_1^+ \rangle$ | – | 0 | – | – | – | – | 0 |
| | $\langle 2_1^+ \|\| E2 \|\| 4_4^+ \rangle \langle 4_4^+ \|\| E2 \|\| 2_1^+ \rangle$ | – | – | – | – | – | – | 0 |
| | $\langle 2_1^+ \|\| E2 \|\| 3_1^+ \rangle \langle 3_1^+ \|\| E2 \|\| 2_1^+ \rangle$ | – | 30 | – | – | – | – | 2 |
| | $\langle 2_1^+ \|\| E2 \|\| 2_1^+ \rangle \langle 2_1^+ \|\| E2 \|\| 2_1^+ \rangle$ | 430 | 430 | 430 | 620 | 140 | 220 | 5 |
| | $\langle Q^2 \rangle$ | 6600(400) | 5980 | 5860 | 7100 | 4130 | 7020 | 8090 |
| | $\langle \beta \rangle$ | 0.17(2) | 0.16 | 0.16 | 0.18 | 0.13 | 0.18 | 0.19 |
| | Component $E2 \times E2 \times E2$ | | | Contribution to $\langle Q^3 \cos(3\delta) \rangle$ (e$^3$fm$^6$) | | | | |
| $0_1^+$ | $\langle 0_1^+ \|\| E2 \|\| 2_1^+ \rangle \langle 2_1^+ \|\| E2 \|\| 2_1^+ \rangle \langle 2_1^+ \|\| E2 \|\| 0_1^+ \rangle$ | -312050 | -219300 | -194100 | -376403 | -106600 | -225700 | -36800 |
| | $\langle 0_1^+ \|\| E2 \|\| 2_2^+ \rangle \langle 2_2^+ \|\| E2 \|\| 2_2^+ \rangle \langle 2_2^+ \|\| E2 \|\| 0_1^+ \rangle$ | 450 | 2100 | 800 | 4400 | 300 | 1050 | 10 |
| | $\langle 0_1^+ \|\| E2 \|\| 2_3^+ \rangle \langle 2_3^+ \|\| E2 \|\| 2_3^+ \rangle \langle 2_3^+ \|\| E2 \|\| 0_1^+ \rangle$ | 2 | -70 | – | – | – | – | -300 |
| | $\langle 0_1^+ \|\| E2 \|\| 2_4^+ \rangle \langle 2_4^+ \|\| E2 \|\| 2_4^+ \rangle \langle 2_4^+ \|\| E2 \|\| 0_1^+ \rangle$ | 0 | – | – | – | – | – | 0 |
| | $\langle 0_1^+ \|\| E2 \|\| 2_1^+ \rangle \langle 2_1^+ \|\| E2 \|\| 2_2^+ \rangle \langle 2_2^+ \|\| E2 \|\| 0_1^+ \rangle$ | 45100 | 40800 | 17700 | 64500 | 15700 | 44800 | -19700 |
| | $\langle 0_1^+ \|\| E2 \|\| 2_1^+ \rangle \langle 2_1^+ \|\| E2 \|\| 2_3^+ \rangle \langle 2_3^+ \|\| E2 \|\| 0_1^+ \rangle$ | -4700 | -700 | – | – | – | – | -900 |
| | $\langle 0_1^+ \|\| E2 \|\| 2_1^+ \rangle \langle 2_1^+ \|\| E2 \|\| 2_4^+ \rangle \langle 2_4^+ \|\| E2 \|\| 0_1^+ \rangle$ | 2700 | – | – | – | – | – | 0 |
| | $\langle 0_1^+ \|\| E2 \|\| 2_2^+ \rangle \langle 2_2^+ \|\| E2 \|\| 2_3^+ \rangle \langle 2_3^+ \|\| E2 \|\| 0_1^+ \rangle$ | – | 400 | – | – | – | – | -600 |
| | $\langle 0_1^+ \|\| E2 \|\| 2_2^+ \rangle \langle 2_2^+ \|\| E2 \|\| 2_4^+ \rangle \langle 2_4^+ \|\| E2 \|\| 0_1^+ \rangle$ | 500 | – | – | – | – | – | 1 |
| | $\langle \cos(3\delta) \rangle$ | 0.4(2) | 0.3 | 0.5 | 0.4 | 0.3 | 0.2 | 0.1 |
| | $\langle \gamma \rangle$ | 23(5)° | 23° | 20° | 23° | 25° | 26° | 28° |

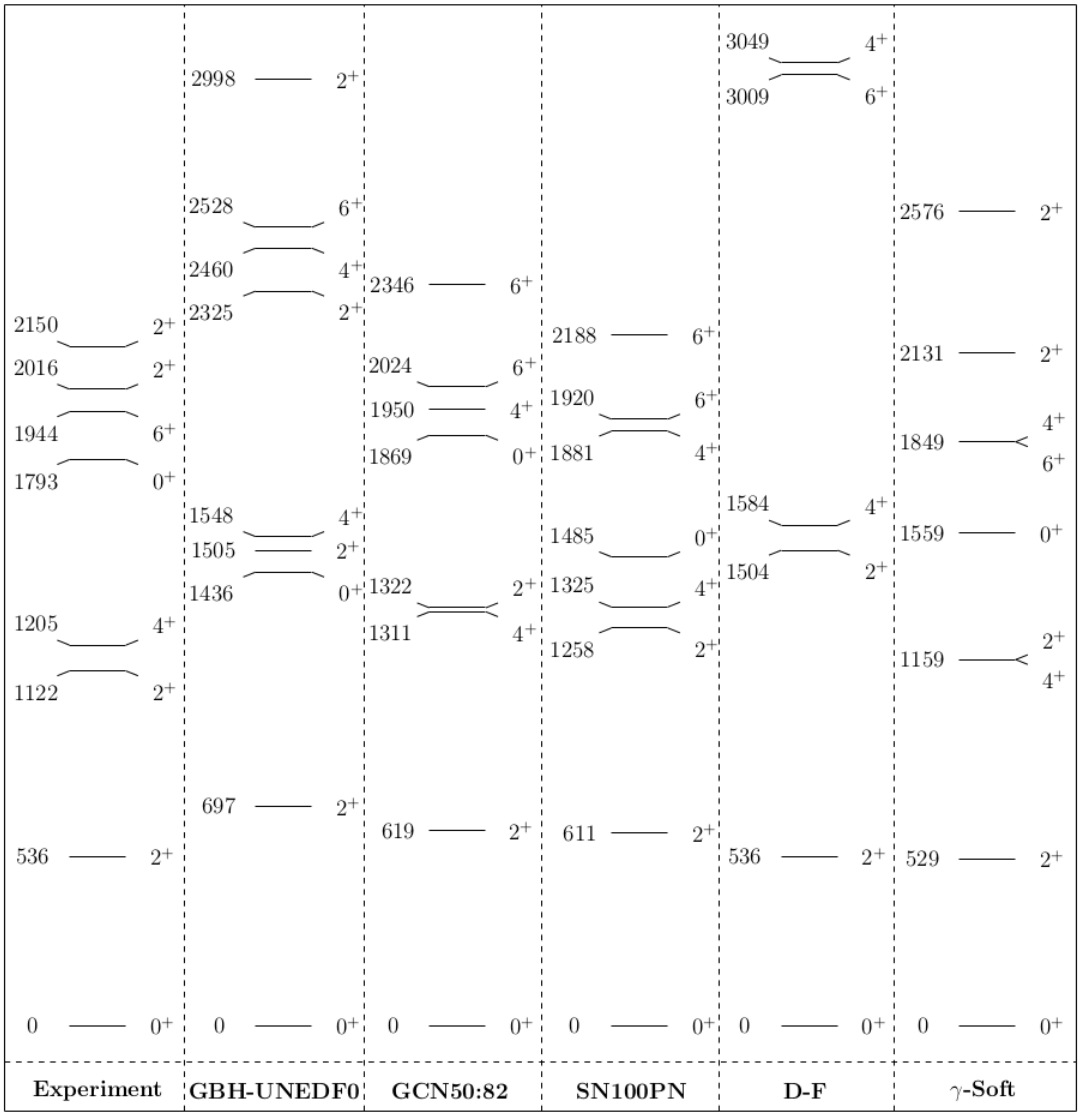


FIG. 6: (Color online) Experimental [3] and theoretical low-lying energy level schemes for $^{130}$Xe. See the text for the details of the calculations.

compared with both the values of the experimentally determined matrix elements, and the $\gamma$ value determined in the quadrupole sum-rules analysis for the $^{130}$Xe ground state. The agreement between model predictions and experimental results is depicted by the overlap region, which again points to the significant degree of traxiality for the ground state.

*$\gamma$-soft model*

Finally, the experimental results were compared to the results of calculations performed with a phenomenological $\gamma$-soft model. This approach is based on a Hamiltonian with $\gamma$-independent potential energy and a constant mass parameter [2, 38]. It is a generalization of the Wilets–Jean model (W-J) [61] for a full range of $\beta$ deformation. The W-J model assumes large beta deformation, while the $\gamma$-soft model [2] describes a smooth transition from the standard quadrupole vibrational model through to large beta deformation, and therefore gives the possibility of rather simple classification of collective excitation in terms of quantum numbers responsible for different modes of excitation: $n_\beta$, number of $\beta$ vibrational phonons, and $\lambda$, describing coupled rotational and $\gamma$-vibrational excitations. It also provides several useful selection rules for the electric quadrupole transitions (see, for instance, the case of $^{140}$Sm presented in Ref. [62]). The beta potential part is described with the following formula:

$$V(\beta,\gamma) = C\cdot\beta^2/2 + G\cdot(exp(-\beta^2/a^2) - 1) +$$

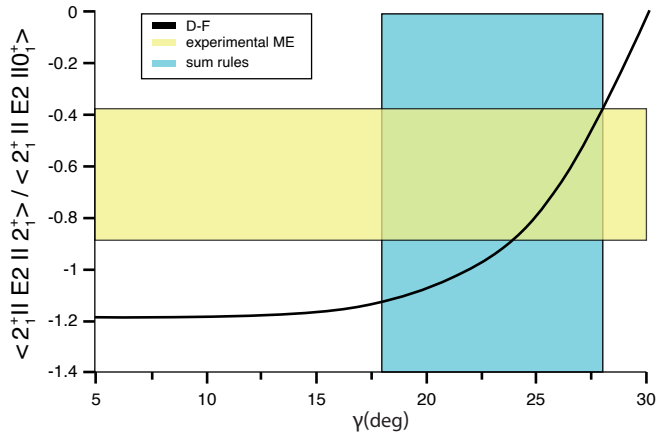


FIG. 7: (Color online) The diagonal matrix element $\langle 2_1^+||E2||2_1^+\rangle$ in $^{130}$Xe, normalized to the $\langle 2_1^+||E2||0_1^+\rangle$ transitional matrix element, as a function of the $\gamma$ deformation parameter [60]. The solid black line represents the results of the Davydov-Filippov model, the yellow shaded area corresponds to the values of matrix elements determined in the present study (with $1\sigma$ uncertainty), and the blue shaded area shows the result of the quadrupole sum rules analysis for the $^{130}$Xe ground state.

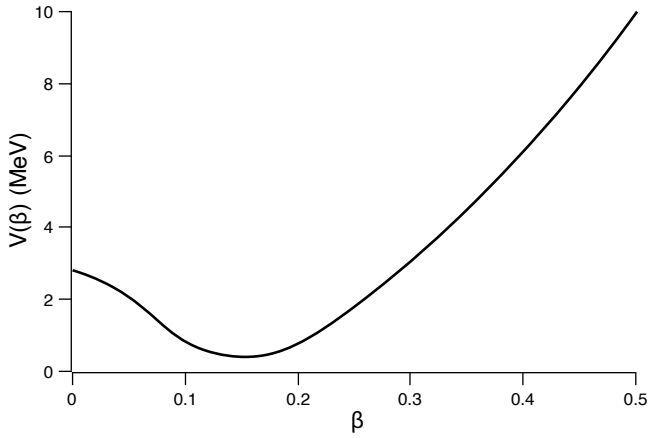


FIG. 8: (Color online) Plot of the potential energy function (1), used in the phenomenological $\gamma$-soft collective model.

$$+f \cdot \beta^3 cos3\gamma \qquad (1)$$

with C = 90 MeV, a = 0.10, G = 3.816 MeV, f = -2 (see Figure 8), and with mass parameter B = 150 $\hbar^2$/MeV (more precisely $B_{\beta\beta} = B_{\gamma\gamma} = B_x = B_y = Bz = B$ and $B_{\beta\gamma} = 0$). The last term of the equation may be treated as a perturbation.

The parameters of the model were adjusted in a few steps, starting from those for $^{130}$Xe taken from Ref. [2], in order to reproduce the experimental level energies (see Figure 6), including the first excited $0^+$ states. Notably, the calculated B($E2$) values are also reproduced reasonably well.

The matrix elements calculated with this model are given in Tables III and IV and, furthermore, the calculations indicate mean $\beta$ deformations of 0.18, 0.19, 0.21 and 0.21 for the $0_1^+$, $2_1^+$, $4_1^+$ and $2_2^+$ states, respectively. The model yields maximum $\gamma$ softness for all states, as a result of gamma independent potential energy surface.

## V. CONCLUSIONS

The nucleus $^{130}$Xe was studied in a Coulomb-excitation experiment performed at CERN's HIE-ISOLDE facility. A set of matrix elements was obtained from the measured $\gamma$-ray yields connecting low-lying states, and included the first measurement of spectroscopic quadrupole moments in this nucleus. These experimental results are well reproduced by both the GBH calculations, using the UNEDF0 functional as a microscopic input, and by large-scale shell-model calculations, performed with both the GCN50:82 and SN100PN interactions. In particular, it was found that the mean-field calculations were able to reproduce the collective properties, e.g. transition strengths and quadrupole moments, well but required a significant scaling factor in order to reproduce the observed energy spectrum. On the other hand, the shell-model calculations required large effective charges to reproduce the transition strengths but matched the energy spectrum well. Nevertheless, these results point to the presence of the triaxial degree of freedom in the low-lying level structure, a feature which was investigated further with the quadrupole sum rule approach. Here, the sets of both the experimental and theoretical $E2$ matrix elements were converted into deformation parameters ($\beta$,$\gamma$), for the ground state. The results indicate modest prolate deformation with significant triaxiality.

Finally, both the experimental and theoretical results were compared to those obtained with a simple Davydov-Filippov model, which struggled to reproduce matrix elements related to the $2_2^+$ state, and a $\gamma$-soft model, based on a Hamiltonian with a $\gamma$-independent potential energy surface which naturally yields quadrupole moments close to zero, in disagreement with the experimental data. It is clear, therefore, that neither the $\gamma$-rigid or $\gamma$-soft model provides an adequate description of $^{130}$Xe.

Although the GBH calculations point towards $\gamma$ softness rather than rigid triaxial deformation for the ground state (see Figure 5), firm conclusions from experimental data are difficult to obtain. We note also that the theoretical $\langle\cos(3\delta)\rangle$ invariants calculated for the $\gamma$-rigid and $\gamma$-soft deformation are very close to each other ($\langle\cos_{\mathtt{soft}}(3\times 23^\circ)\rangle = 0.92$ and $\langle\cos_{\mathtt{rigid}}(3\times 28^\circ)\rangle = 0.88$). Conclusions related to $\gamma$-rigid and $\gamma$-soft deformation would require a sufficiently rich set of matrix elements to be obtained such that the $\langle Q^6\cos^2(3\delta)\rangle$ invariant could

be reliably determined, which is related to the dispersion in $\gamma$, and a future experimental study of $^{130}$Xe could similarly obtain the necessary matrix elements.

Such a study would also populate excited $0^+$ states which represent key daughter levels for the decay of $0\nu\beta\beta$ candidate $^{130}$Te.

## VI. ACKNOWLEDGEMENTS

The authors would like to thank the HIE-ISOLDE accelerator division for the beam, and members of the MINIBALL collaboration for their hard work on the project.

We would like to thank Chrystian Droste and Grzegorz Rohoziński for the discussions on the structure of $^{130}$Xe.

The research leading to these results has received funding from the European Union's Horizon 2020 research and innovation programme under grant agreement no. 654002 + 665779 CERN (COFUND). Support from Science and Technology Facilities Council (UK) through grants ST/P005314/1, ST/L005743/1, ST/R004056/1, and ST/J000051/1, and German BMBF under contract 05P18PKCIA + 'Verbundprojekt' 05P2018 are acknowledged.

[1] L. Próchniak, Phys. Scr. **90**, 114005 (2015).
[2] S. G. Rohoziński, J. Srebrny, and K. Horbaczewska, Zeit. für Physik **268**, 401 (1974).
[3] B. Singh, Nucl. Data Sheets **93** (2001).
[4] N. Hinohara, Z. P. Li, T. Nakatsukasa, T. Nikšić, and D. Vretenar, Phys. Rev. C **85**, 024323 (2012).
[5] D. Bonatsos, P. E. Georgoudis, N. Minkov, D. Petrellis, and C. Quesne, Phys. Rev. C **88**, 034316 (2013).
[6] A. I. Budaca and R. Budaca, Phys. Rev. C **101**, 064318 (2020).
[7] X. F. Meng, F. R. Wang, Y. A. Luo, F. Pan, and J. P. Draayer, Phys. Rev. C **77**, 047304 (2008).
[8] K. Nomura, T. Nikšić, and D. Vretenar, Phys. Rev. C **96**, 014304 (2017).
[9] K. Nomura, R. Rodríguez-Guzmán, and L. M. Robledo, Phys. Rev. C **96**, 064316 (2017).
[10] P. von Brentano, A. Gelberg, S. Harissopulos, and R. F. Casten, Phys. Rev. C **38**, 2386 (1988).
[11] L. Coquard et al., Phys. Rev. C **82**, 024317 (2010).
[12] W. Maneschg, Nucl. and Part. Phys. Proc. **260**, 188 (2015).
[13] T. R. Rodríguez and G. Martínez-Pinedo, Phys. Rev. Lett. **105**, 252503 (2010).
[14] P. Schmidt, F. Ames, G. Bollen, O. Forstner, G. Huber, M. Oinonen, and J. Zimmer, Nucl. Phys. A **701**, 550 (2002).
[15] L. Morrison et al., in Proceedings of the Journal of Physics: Conference Series, Glasgow (2020), in press.
[16] M. J. G. Borge and K. Riisager, Eur. Phys. J. A **52**, 334 (2016).
[17] Y. Kadi, Y. Blumenfeld, W. V. Delsolaro, M. A. Fraser, M. Huyse, A. P. Koufidou, J. A. Rodriguez, and F. Wenander, J. Phys. G **44**, 084003 (2017).
[18] D. Cline, Annu. Rev. Nucl. Part. Sci. **36**, 683 (1986).
[19] N. Warr et al., Eur. Phys. J. A **49**, 1 (2013).
[20] A. Ostrowski, S. Cherubini, T. Davinson, D. Groombridge, A. Laird, A. Musumarra, A. Ninane, A. Di Pietro, A. Shotter, and P. Woods, Nucl. Instrum. Methods **480**, 448 (2002).
[21] L. P. Gaffney (2018), available at: `https://github.com/lpgaff/kinsim/blob/master/kinsim3.cc`.
[22] A. E. Kavka, *Ph.D. thesis, University of Uppsala* (1990).
[23] L. Morrison, *Ph.D. thesis, University of Surrey* (to be submitted 2020).
[24] Z. Elekes and J. Timar, Nucl. Data Sheets **129**, 191 (2015).
[25] T. Czosnyka, D. Cline, and C. Y. Wu, Bull. Am. Phys. Soc. **28**, 745 (1982), available at: `http://slcj.uw.edu.pl/en/gosia-code/`.
[26] M. Zielińska, L. P. Gaffney, K. Wrzosek-Lipska, E. Clément, T. Grahn, N. Kesteloot, P. Napiorkowski, J. Pakarinen, P. Van. Duppen, and N. Warr, Eur. Phys. J. A **52**, 99 (2016), ISSN 1434-601X.
[27] D. Abriola and A. A. Sonzogni, Nucl. Data Sheets **107**, 2423 (2006).
[28] L. P. Gaffney (2019), available at: `https://github.com/lpgaff/chisqsurface`.
[29] T. Konstantinopoulos et al., HNPS Adv. Nucl. Phys. **19**, 33 (2011).
[30] T. Konstantinopoulos, *Ph.D. thesis, National Technical University of Athens (NTUA)* (2012).
[31] G. Jakob et al., Phys. Rev. C **65**, 024316 (2002).
[32] S. Raman, C. Nestor, and P. Tikkanen, At. Data Nucl. Data Tables **78**, 1 (2001).
[33] W. F. Mueller, M. P. Carpenter, J. A. Church, D. C. Dinca, A. Gade, T. Glasmacher, et al., Phys. Rev. C **73**, 014316 (2006).
[34] S. A. Hamada, W. D. Hamilton, and B. More, J Phys G: Nucl **14**, 1237 (1988).
[35] E. E. Peters et al., Phys. Rev. C **94**, 024313 (2016).
[36] N. J. Stone, At. Data Nucl. Data Tables **111-112**, 1 (2016), ISSN 0092-640X.
[37] A. Davydov and G. Filippov, Nucl. Phys. **8**, 237 (1958).
[38] L.Goettig et al., Nucl. Phys. A **357**, 109 (1981).
[39] M. Kortelainen, T. Lesinski, J. Moré, W. Nazarewicz, J. Sarich, N. Schunck, M. V. Stoitsov, and S. Wild, Phys. Rev. C **82**, 024313 (2010).
[40] L. Próchniak, P. Quentin, D. Samsoen, and J. Libert, Nucl. Phys. A **730**, 59 (2004), ISSN 0375-9474.
[41] K. Wrzosek-Lipska et al., Phys. Rev. C **86**, 064305 (2012).
[42] L. Próchniak and S. G. Rohoziński, J. Phys. G **36**, 123101 (2009).
[43] P.-G. Reinhard and H. Flocard, Nucl. Phys. A **584**, 467 (1995), ISSN 0375-9474.
[44] E. Caurier, F. Nowacki, A. Poves, and K. Sieja, Phys. Rev. C **82**, 064304 (2010).
[45] B. A. Brown, N. J. Stone, J. R. Stone, I. S. Towner, and M. Hjorth-Jensen, Phys. Rev. C **71**, 044317 (2005).
[46] B. A. Brown and W. D. M. Rae, Nucl. Data Sheets **120**, 115 (2014).
[47] N. Shimizu, *Nuclear shell-model code for massive parallel computation, "KSHELL"* (2013).
[48] L. Kaya, A. Vogt, P. Reiter, M. Siciliano, B. Birkenbach,

A. Blazhev, L. Coraggio, E. Teruya, N. Yoshinaga, and K. Higashiyama, Phys. Rev. C **98**, 014309 (2018).
[49] A. Vogt et al., Phys. Rev. C **96**, 024321 (2017).
[50] L. Kaya et al., Phys. Rev. C **98**, 054312 (2018).
[51] L. Kaya, A. Vogt, P. Reiter, C. Müller-Gatermann, A. Gargano, L. Coraggio, N. Itaco, A. Blazhev, et al., Phys. Rev. C **99**, 014301 (2019).
[52] A. Vogt, B. Birkenbach, P. Reiter, A. Blazhev, M. Siciliano, K. Hadyńska-Klęk, J. J. Valiente-Dobón, C. Wheldon, E. Teruya, and N. Yoshinaga, Phys. Rev. C **95**, 024316 (2017).
[53] J. Katakura and K. Kitao, Nucl. Data Sheets **97**, 765 (2002).
[54] N. J. Stone, At. Data Nucl. Data Tables **90**, 75 (2005).
[55] K. Kumar, Phys. Rev. Lett. **28**, 249 (1972).
[56] J. Srebrny and D. Cline, Int. J. Mod. Phys. E. **20**, 422 (2011).
[57] K. Hadyńska-Klęk et al., Phys. Rev. C **97**, 024326 (2018).
[58] P. L.Próchniak, HIL Annual Report 2015 p. 82 (2016).
[59] P. Napiorkowski (2016), '`DFcode`' available at: `www.kody.slcj.uw.edu.pl`.
[60] E. Clément et al., Phys. Rev. C **94**, 054326 (2016).
[61] L. Wilets and M. Jean, Phys. Rev. **102**, 788 (1956).
[62] J. Samorajczyk, L. Próchniak, J. Srebrny, C. Droste, S. Rohozinski, and the EAGLE collaboration, HIL Annual Report 2019 p. 66 (2020), available at: `http://slcj.uw.edu.pl/wp-content/uploads/2020/06/HIL_Raport2019.pdf`.